Regular Article

Generalized fractal dimensions based comparison analysis of edge detection methods in CT images for estimating the infection of COVID-19 disease

C. Thangaraj[a] and D. Easwaramoorthy[b]

Department of Mathematics, School of Advanced Sciences, Vellore Institute of Technology, Vellore, Tamil Nadu, India

Abstract The coronavirus, also known as COVID-19, has become highly contagious and has been associated with one of the world's deadliest diseases. It also has direct effects on human lungs, causing significant damage. CT-scans are commonly employed in such circumstances to promptly evaluate, detect, and treat COVID-19 patients. Without any filtering, CT-scan images are more difficult to identify the damaged parts of the lungs and determine the severity of various diseases. In this paper, we use the multifractal theory to evaluate COVID-19 patient's CT-scan images to analyze the complexity of the various patient's original, filtered, and edge detected CT-scan images. To precisely characterize the severity of the disease, the original, noisy and denoised images are compared. Furthermore, the edge detection and filtered methods called Robert, Prewitt, and Sobel are applied to analyze the various patient's COVID-19 CT-scan images and examined by the multifractal measure in the proposed technique. All of the images are converted, filtered and edge detected using Robert, Prewitt, and Sobel edge detection algorithms, and compared by the Generalized Fractal Dimensions are compared. For the CT-scan images of COVID-19 patients, the various Qualitative Measures are also computed exactly for the filtered and edge detected images by Robert, Prewitt, and Sobel schemes. It is observed that Sobel method is performed well for classifying the COIVD-19 patients' CT-scans used in this research study, when compared to other algorithms. Since the image complexity of the Sobel method is very high for all the images and then more complexity of the images contains more clarity to confirm the COVID-19 images. Finally, the proposed method is supported by ANOVA test and box plots, and the same type of classification in experimental images is explored statistically.

1 Introduction

The fractal is a geometric pattern with an irregular design. It is found with a uniform irregularity at each level. In addition, it is considered a rigid fragmentary geometric structure. In addition, these are seen as a whole reduced copy. A further fractal is an infinite number of forms and of innumerable complexities. These can be found in different sizes and with the same shape.

Furthermore, the fractal was mathematically defined by the Mandelbrot in 1975, i.e., Hausdorff dimension exceeds (strictly) the topological dimension [1]. He was also the first to introduce fractal geometry. The word fractal is derived from the Latin word fractus, which means broken. Fractal geometry is used to estimate many natural objects and their complex properties to a certain extent more than other geometric methods [2, 3]. That is, fractal geometry is a useful method for estimating natural objects, such as mountains, clouds, vegetables, beaches and trees. It is also used to model natural structure, image abstraction, analysis of clinical diagnostic images, and study confusing phenomena [4]. The fractal dimension also helps to describe the traditional image processing and structure of the images. Furthermore, the function of the fractal dimension is excellent in image analysis [5].

Fractal dimension analyzes the irregularity of the given object with homogeneous scaling properties. The concept of fractal dimension can be practicable in the measurement and categorization of shape and texture. Numerous research works have been described in medical image analysis employing fractal analysis [7]. Fractal dimension is insufficient to characterize the object as having complex and inhomogeneous scaling properties. In addition, the function of the fractal dimension does not fit into the complex and asymmetric scaling feature [8]– [10]. Therefore, we use the multifractal method GFD to avoid it. GFD seeks to measure the complexity and asymmetry of an image in that reasons GFD to elect an image edge detection. We can

[a] e-mail: ctrmath1@gmail.com

[b] e-mail: easandk@gmail.com (corresponding author)

3718

Eur. Phys. J. Spec. Top. (2022) 231:3717–3739

Table 1 Sample of various COVID-19 patients information

COVID-19 Patient age	Patient sex
35 Years (P1)	Male
40 Years (P2)	Female
45 Years (P3)	Male
45 Years (P4)	Female
50 Years (P5)	Male
60 Years (P6)	Female
65 Years (P7)	Male
70 Years (P8)	Male

apply the GFD method to compare the Sobel, Prewitt and Robert edge detection method's complexity of the various COVID-19 patient's images. The qualitative measure is useful during image processing, distortion caused by noise, blurring, sounds and abstract artifacts will impair image quality [11]–[18]. When doing other qualities with distorted images, the value of the uncompressed image is useful. Using full reference quality data, we can directly compare target and reference images at this point [21]–[23].

COVID-19, a coronavirus infection, was first identified in the Chinese state of Wuhan in 2019 as the largest epidemic the world has ever seen. Its impact is spreading all over the world today and poses a great challenge to mankind. The epidemic has spread to almost all parts of the world and has claimed many lives, questioning their condition and economy. In addition, many have lost their lives and lost close relationships. The onset of symptoms is usually mild, with fever, dry cough and extreme tiredness followed by normal medical treatment which increases the severity of the infection and then reduces the oxygen level in the body [24]. It is considered a deadly disease. Today, the World Health Organization (WHO) says that the number of COVID-19 victims worldwide at 452201564 and the number of deaths at 6029852 as of 12 March 2022. In the last 24 h alone, the number of new victims on 13 March 2022 was 149088. In addition, the most affected countries worldwide are 78739443 persons in the United States of America, 42984261 persons in India, 29249903 persons in Brazil, 22614907 persons in France, 19457980 persons in the United Kingdom and 17242043 persons in Russia. Its number is increasing day by day.

Many researchers and physicians are spending a lot of time and money trying to find a way to control the spread of COVID-19 and prevent it from spreading completely today. But even though some vaccines today have somewhat reduced that spread, the virus continues to undermine the function of the vaccine due to various genetic mutations [25]–[27]. So that the number of spreads decreases and suddenly increases. It is, therefore, imperative to know in advance the severity of the infection. This is because COVID-19 can only prevent life-threatening damage if it is clearly diagnosed and treated before the disease progresses. Although the

RT-PCR device may function as a predictor, its function is not suitable for monitoring human lung function. That is why computer tomography (CT)-scan technology is used as a tool to explain the function of the lungs [28]–[30]. It can explain the severity of the infection in the human lungs. However, CT-scan and X-ray images are commonly used in medical technology. To describe such images we hope to simplify the nature of this type of complication and then explain the severity of the infection more clearly with the procedure multifractal procedure commonly used in medicine today. The complexity of the images can be easily explained using GFD, especially in the multifractal model. Therefore, multifractal detection of disease severity using COVID-19, X-ray and CT chest Scan images is now widely used by many researchers [31]–[34].

To describe an object with complicated and inhomogeneous scaling properties, the monofractal dimension is insufficient in certain places. Monofractal and correlation dimensional measures are the most accessible non-linear tools for processing the real-world experimental images. A single-dimensional metric cannot describe the image's non-uniformity or inhomogeneity. This dimensional scale is insufficient to classify the randomness or inconsistency of the experimental image. The Generalized Fractal Dimensions (GFD) or Renyi Fractal Dimensions define a Multifractal as an inhomogeneous set. The GFD is used to assess, characterize, and quantify the irregular structure of the realistic signals and images. In general, the physicians are unable to clearly assess, examine, and segment the interior appearances and infected parts of the lungs. Because the lung includes multiple lobe systems with intricate structures and it is quite challenging to describe the interior appearances, patterns, and damaged sections of the patient's lung. CT-scan images are widely utilized in the medical field and it is highly sophisticated grayscale images used to examine the lungs. As the human lung is a multicomplex system, the analysis of CT-scan lung images leads to face certain difficulties, particularly for physicians. To analyze and examine the complex CT-scan lung images, the nonlinear methods such as GFD measure can be applied to determine the nature and severity of the disease through the efficient image processing tools. The multifractal measure is able to evaluate, characterize, and quantify the irregular medical images, and to detect the noise levels in complicated images. Hence, the multifractal concept is applied in CT-scan images of our human lungs.

As the main features of this article, the GFD variation using different Edge detection methods are systematically explained. In addition, then, the various qualitative measures of the Sobel, Robert and Prewitt edge detected images are computed and illustrated. The rest of this paper is organized with the following structure. In Sect. 2, the methods used in this paper such as the GFD method, and Prewitt, Robert and Sobel edge detection methods are explained and also the image qualitative measures, ANOVA test and algorithmic structure of the proposed scheme are presented. The data collection is elaborated in Sect. 3. The results

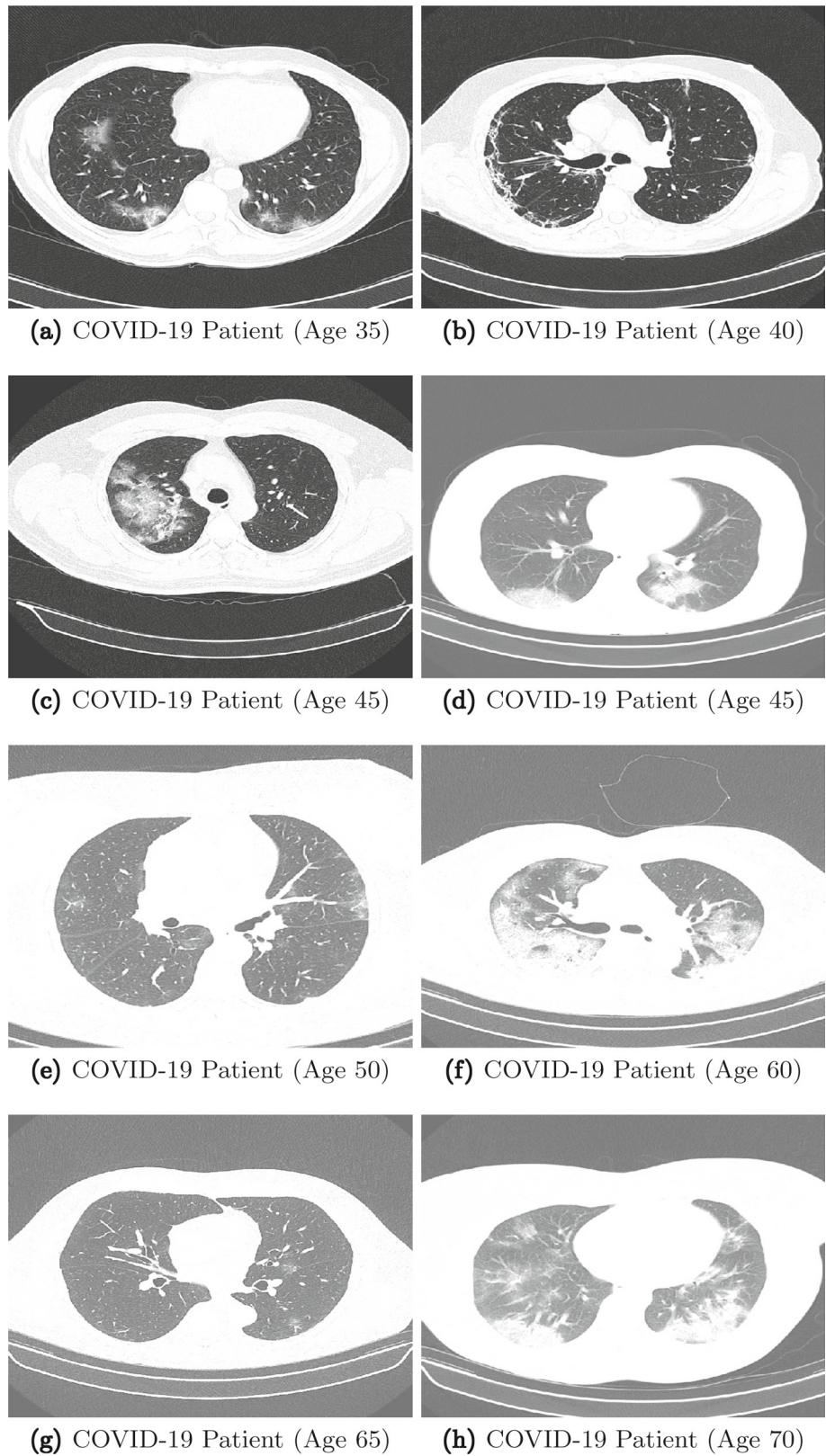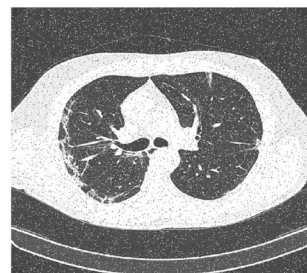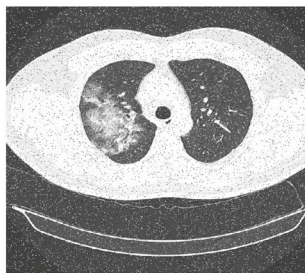**Fig. 1** Sample set of original COVID-19 patients' CT-scan images before preprocessing steps
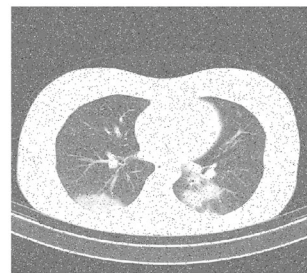

(a) COVID-19 Patient (Age 35)

(b) COVID-19 Patient (Age 40)

(c) COVID-19 Patient (Age 45)

(d) COVID-19 Patient (Age 45)

(e) COVID-19 Patient (Age 50)

(f) COVID-19 Patient (Age 60)

(g) COVID-19 Patient (Age 65)

(h) COVID-19 Patient (Age 70)

Fig. 2 Sample set of noisy
COVID-19 patients'
CT-scan images corrupted
by salt and pepper noise
with density 0.05

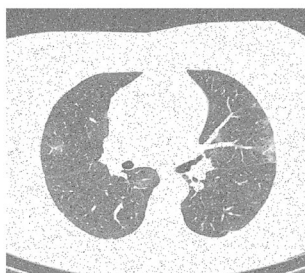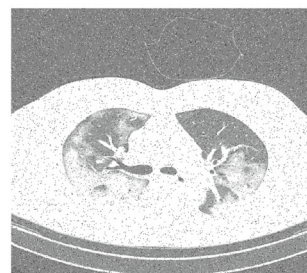**(a)** COVID-19 Patient (Age 35)   **(b)** COVID-19 Patient (Age 40)
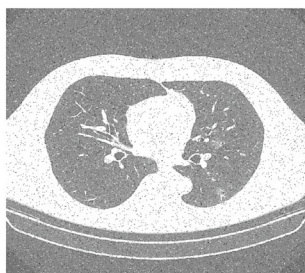
(c) COVID-19 Patient (Age 45)   **(d)** COVID-19 Patient (Age 45)
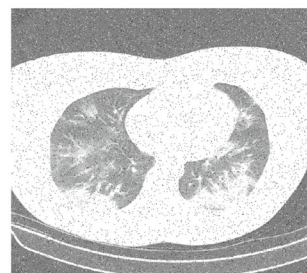
(e) COVID-19 Patient (Age 50)   **(f)** COVID-19 Patient (Age 60)

(g) COVID-19 Patient (Age 65)   **(h)** COVID-19 Patient (Age 70)

and discussions of this research framework are explored well in Sect. 4. The conclusion of this study is mentioned in Sect. 5.

2 Methods

As a nonlinear measure to analyze the complex oriented medical images, the Renyi entropy-based multifractal
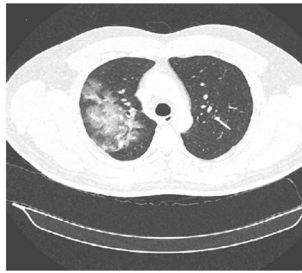
Fig. 3 Sample set of denoised COVID-19 patients' CT-scan images using median filter
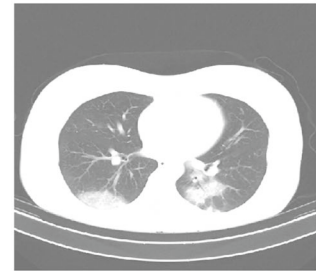

(a) COVID-19 Patient (Age 35)
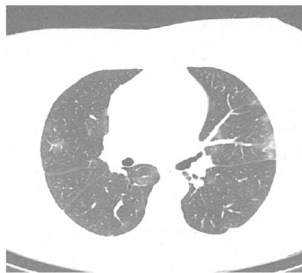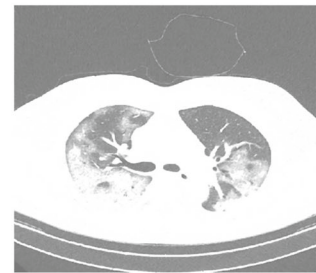
(b) COVID-19 Patient (Age 40)

(c) COVID-19 Patient (Age 45)

(d) COVID-19 Patient (Age 45)

(e) COVID-19 Patient (Age 50)

(f) COVID-19 Patient (Age 60)

(g) COVID-19 Patient (Age 65)

(h) COVID-19 Patient (Age 70)

3722

Eur. Phys. J. Spec. Top. (2022) 231:3717–3739

Fig. 4 Comparison of GFD spectra of original, noisy and denoised COVID-19 patients' CT-scan images (Figs. 1, 2 and 3)

(a) COVID-19 Patient (Age 35)

(b) COVID-19 Patient (Age 40)
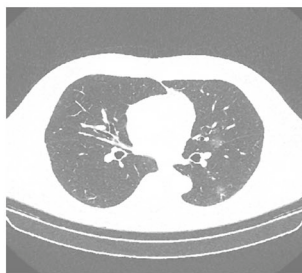
(c) COVID-19 Patient (Age 45)
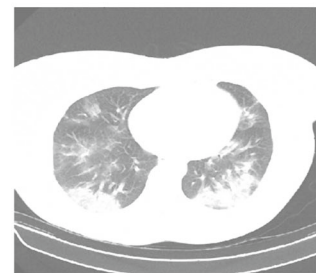
(d) COVID-19 Patient (Age 45)

(e) COVID-19 Patient (Age 50)

(f) COVID-19 Patient (Age 60)

(g) COVID-19 Patient (Age 65)

(h) COVID-19 Patient (Age 70)

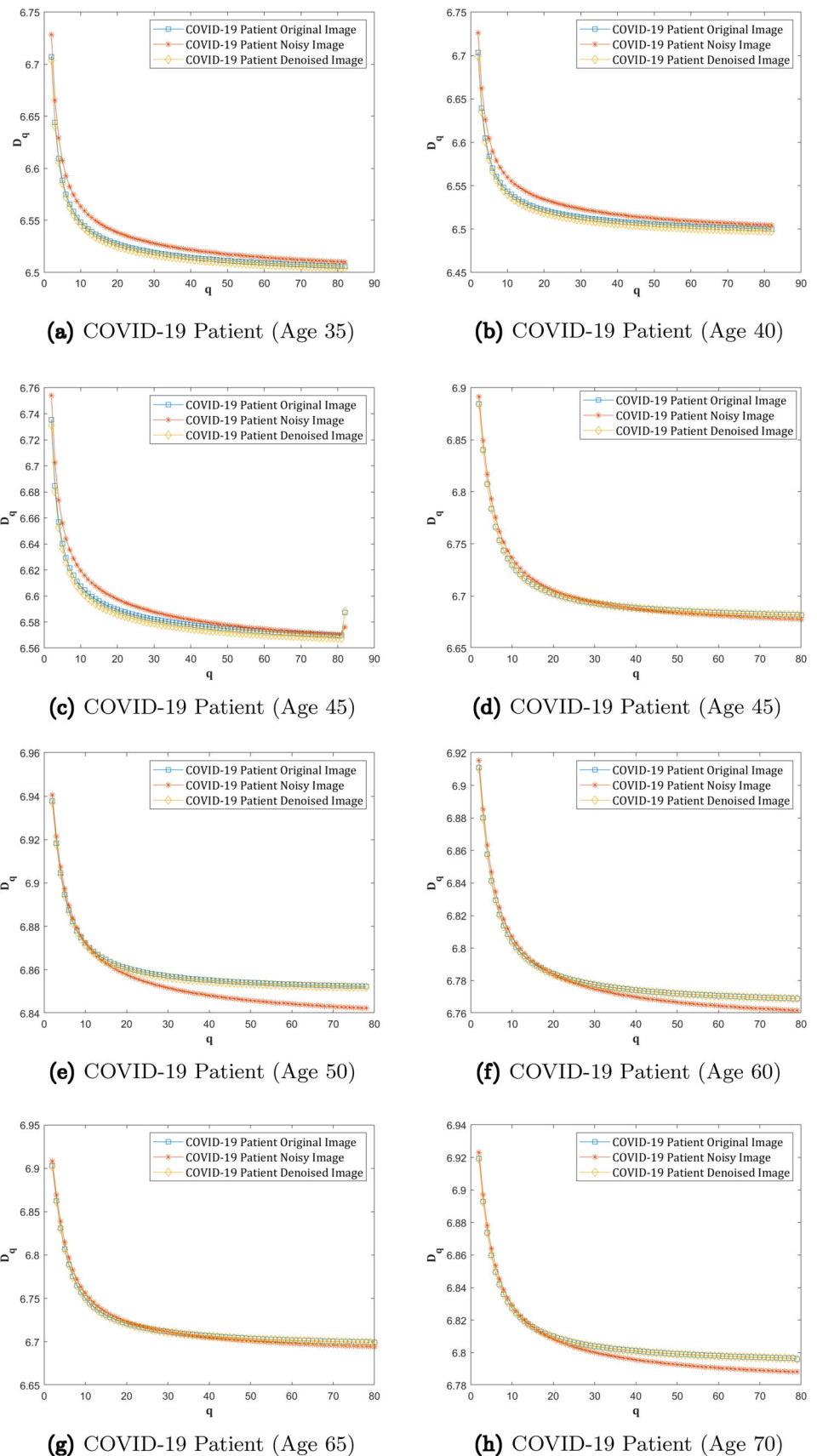Eur. Phys. J. Spec. Top. (2022) 231:3717–3739

3723

Table 2 Comparison of denoising performances of tested CT-scan images

Patients	Noisy image corrupted by salt and pepper noise with density 0.05		Denoised image using median filter	
	MAE	PSNR	MAE	PSNR
P1	6.3513	17.1492	6.6551	26.9766
P2	6.4059	17.6507	1.8419	35.3122
P3	6.3449	17.2388	5.3104	28.8595
P4	6.3835	17.1735	2.0780	34.3254
P5	6.4097	17.2988	2.6637	32.8392
P6	6.3673	16.9066	2.5694	32.1822
P7	6.3953	17.1853	5.2210	28.4865
P8	6.3385	17.7366	4.6345	28.7615

measure, called Generalized Fractal Dimensions, is defined in this section as a significant feature of this proposed scheme. Renyi entropy is a very important tool for generalizing the fractal dimension, as it is a typical nonlinear entropy. The multifractal measure, GFD is the most efficient method in nonlinearity analysis to differentiate or estimate the complexity of real-world biomedical images. In addition, the median filter is used to remove the salt and pepper noise introduced in the experimental images, so that the classification rate can be obtained precisely. Furthermore, the three edge detection methods are used in the research work to detect the infected area in the CT-scan lung images of COVID-19 patients. The GFD measure is computed before and after the filtering and detecting edges in the experimental grayscale images with original, noisy and denoised states. To examine the performance of denoising and edge detecting process, the qualitative measures are required in this paper along with the GFD measure. Finally, the obtained classification proportion will be correlated by the statistical tools using the ANOVA test and box plots. Hence, the Renyi entropy, multifractal dimensions, median filter, edge detection methods, qualitative measures and statistical aids are discussed in this section mathematically.

2.1 Renyi entropy

The Renyi entropy was first described by the Hungarian mathematician Alfred Renyi. In addition, the generalized entropy of a given probability distribution is called Renyi entropy. Renyi entropy plays a very important role in further information theory. Furthermore, the generalized fractal dimension can be explained by Renyi entropy [6]–[8].

Whether the Renyi Entropy is given as

$$R_q = \frac{1}{1-q} \log_2 \left(\sum_{i=1}^{N} p_i^q \right) \qquad (1)$$

where $q(\neq 1) \in \mathbb{R}$ is the probability distribution and order. In addition, the given $p_i \in [0,1]$ is the probability of x_i, $i \in \{1, 2, \ldots, N\}$.

2.2 Generalized fractal dimensions for grayscale images

Renyi Entropies are important measures of uncertainty or randomness in nonlinear analysis and statistics. They also result in a range of Fractal Dimension indices (Renyi Fractal Dimensions or Generalized Fractal Dimensions). The generalized fractal dimensions is the foundation of multifractal theory. In this section, we'll show you how to use generalized fractal dimensions to determine the noise level of grayscale images [8]–[10].

Now the GFD can be defined as let N be the number of boxes required to cover the grayscale image being evaluated with box size r. The probability p_i for the the tested grayscale image for ith box of size r is defined as

$$p_i = \frac{M_i}{M}$$

where M_i is the mass of the tested grayscale image included in the corresponding ith box of size r and M is the total mass of the tested grayscale image.

The Renyi Fractal Dimensions or GFD of order $q \in (-\infty, \infty)$ such that $q \neq 1$. For the known probability distribution of the given grayscale image can be constructed as

$$D_q = \lim_{r \to 0} \frac{1}{q-1} \frac{\log_2 \left(\sum_{i=1}^{N} p_i^q \right)}{\log_2 r} \qquad (2)$$

Here D_q is called the generalized Renyi Entropy. If $q = 0$, then $D_0 = -\frac{\log_2 N}{\log_2 \varepsilon}$ is called the Fractal Dimension of the image. If q approaches to 1, D_q converges to $D_1 = \lim_{\varepsilon \to 0} \frac{\sum_{i=1}^{N} p_i \log_2 p_i}{\log_2 \varepsilon}$. This is called Information Dimension of the image. If $q = 2$, then D_q is known as Correlation Dimension of the image. In this particular there exist two limit cases
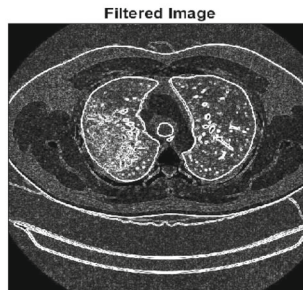
3724

Eur. Phys. J. Spec. Top. (2022) 231:3717–3739

Fig. 5 Sample set of Prewitt filtered CT-scan images for COVID-19 patients
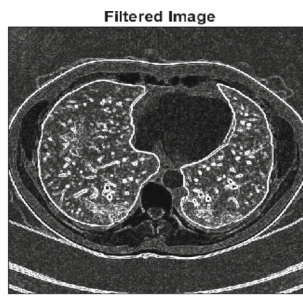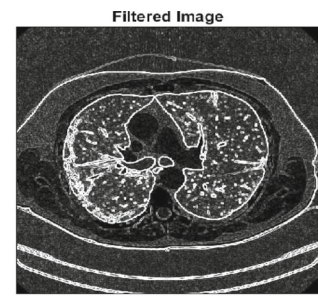
(a) COVID-19 Patient (Age 35)

(b) COVID-19 Patient (Age 40)

(c) COVID-19 Patient (Age 45)

(d) COVID-19 Patient (Age 45)

(e) COVID-19 Patient (Age 50)

(f) COVID-19 Patient (Age 60)

(g) COVID-19 Patient (Age 65)

(h) COVID-19 Patient (Age 70)

Eur. Phys. J. Spec. Top. (2022) 231:3717–3739

3725

Fig. 6 Sample set of Robert filtered CT-scan images for COVID-19 patients
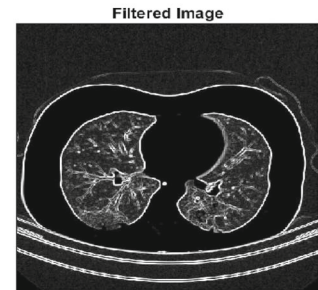

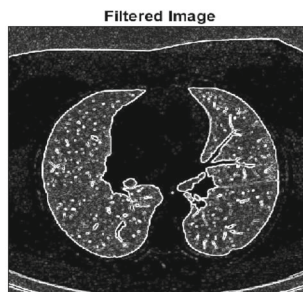**(a)** COVID-19 Patient (Age 35)

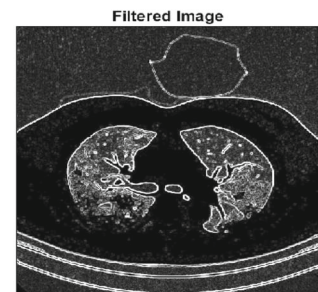**(b)** COVID-19 Patient (Age 40)
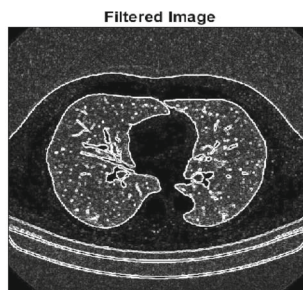

(c) COVID-19 Patient (Age 45)
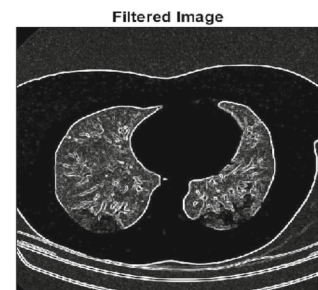

(d) COVID-19 Patient (Age 45)

(e) COVID-19 Patient (Age 50)

(f) COVID-19 Patient (Age 60)

(g) COVID-19 Patient (Age 65)

(h) COVID-19 Patient (Age 70)
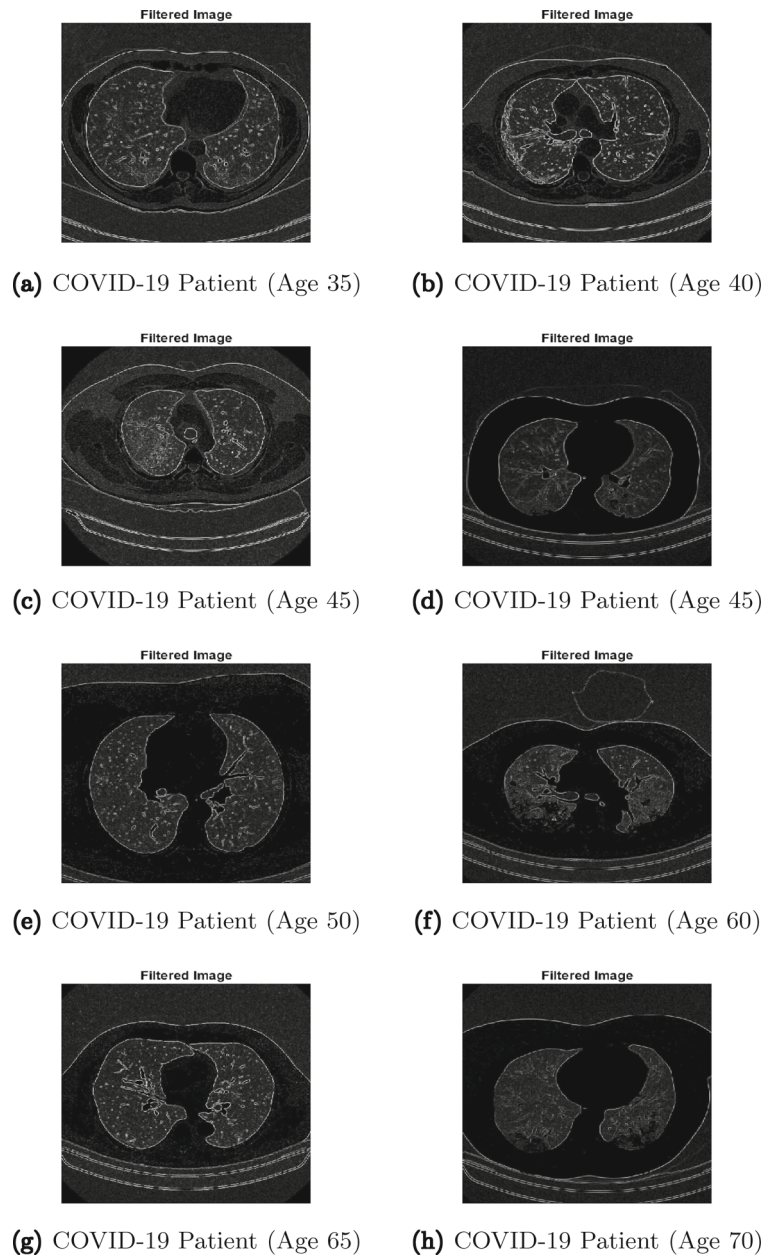
of the image when $q = -\infty$ and $q = \infty$, which is defined as $D_{-\infty} = \lim_{\varepsilon \to 0} \frac{log_2(p_{\min})}{\log_2 \varepsilon}$ and $D_{\infty} = \lim_{\varepsilon \to 0} \frac{\log_2(p_{\max})}{\log_2 \varepsilon}$. Here $p_{\min} = \min\{p_1, p_2, \ldots, p_N\}$ and $p_{\max} = \max\{p_1, p_2, \ldots, p_N\}$.

2.3 Median filter

The noise caused by the electronic noise in the images is usually the noise coming from the scanner and the digital camera. In addition, the noise of the images is described depending on the random variation of color and brightness levels in the image. Similarly, noise refers to unwanted bogus and extraneous information in the image. We also use the median filtration technique to remove unwanted noise. This filtration technique is one

of the very best methods. This technique is a non-linear image processing method that reduces salt and pepper noise. Its functionality is widely used in digital image processing [19]–[21]. The salt and pepper noise was used to produce the original CT-scan grayscale images as noisy images, and the median filter was used to denoise the corrupted original CT-scan grayscale images. To analyze and diagnose conventional CT-scan grayscale images of COVID-19 patients of various ages, we looked at noise levels in the images.

2.4 Edge detection methods

There are two types of edge detection operators one is gradient and another is the Gaussian operator. In this

Fig. 7 Sample set of Sobel filtered CT-scan images for COVID-19 patients
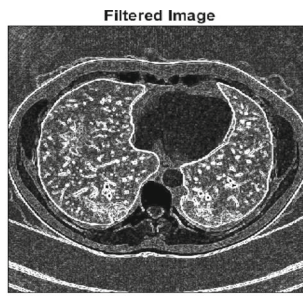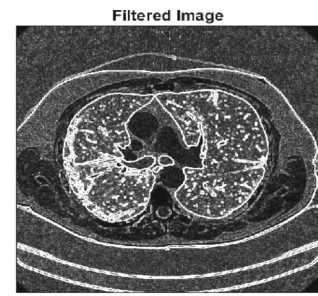
(a) COVID-19 Patient (Age 35)

(b) COVID-19 Patient (Age 40)

(c) COVID-19 Patient (Age 45)

(d) COVID-19 Patient (Age 45)

(e) COVID-19 Patient (Age 50)

(f) COVID-19 Patient (Age 60)

(g) COVID-19 Patient (Age 65)

(h) COVID-19 Patient (Age 70)

Fig. 8 Sample set of
Prewitt edge detected
CT-scan images for
COVID-19 patients
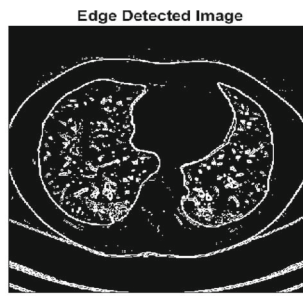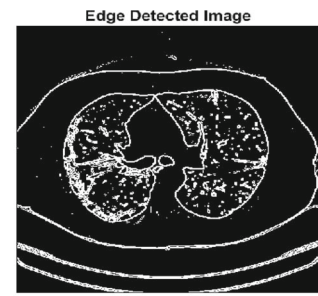
(a) COVID-19 Patient (Age 35)   **(b)** COVID-19 Patient (Age 40)
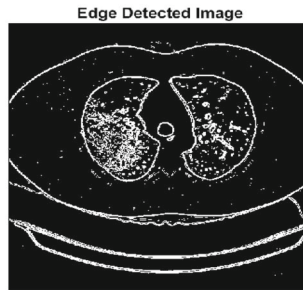
(c) COVID-19 Patient (Age 45)   **(d)** COVID-19 Patient (Age 45)

(e) COVID-19 Patient (Age 50)   **(f)** COVID-19 Patient (Age 60)

(g) COVID-19 Patient (Age 65)   **(h)** COVID-19 Patient (Age 70)

Fig. 9 Sample set of Robert edge detected CT-scan images for COVID-19 patients
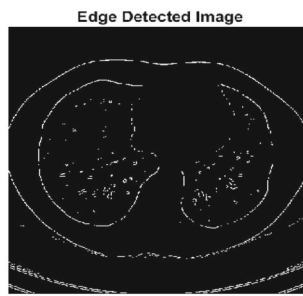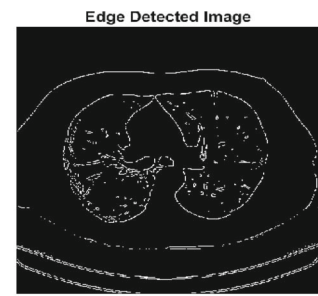
(a) COVID-19 Patient (Age 35)

(b) COVID-19 Patient (Age 40)
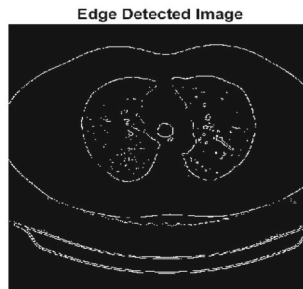
(c) COVID-19 Patient (Age 45)
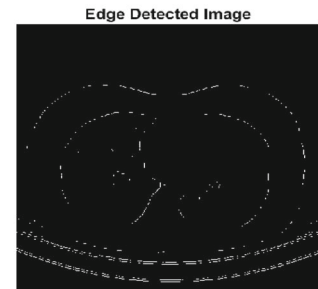
(d) COVID-19 Patient (Age 45)
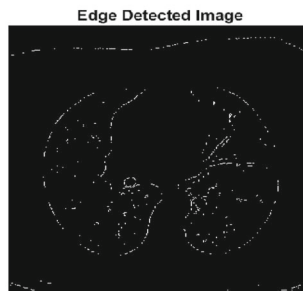
(e) COVID-19 Patient (Age 50)

(f) COVID-19 Patient (Age 60)
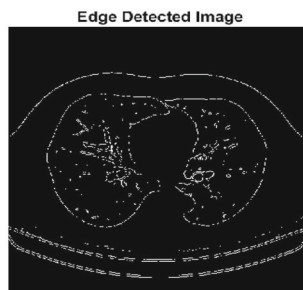
(g) COVID-19 Patient (Age 65)
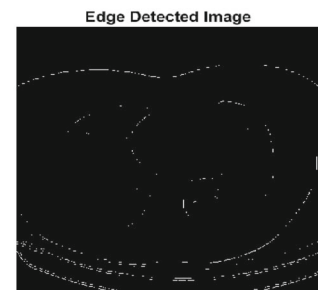
(h) COVID-19 Patient (Age 70)
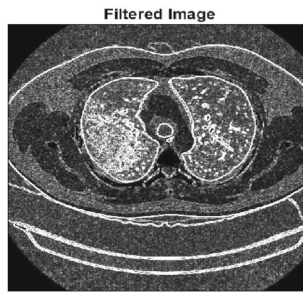
Fig. 10 Sample set of Sobel edge detected CT-scan images for COVID-19 patients
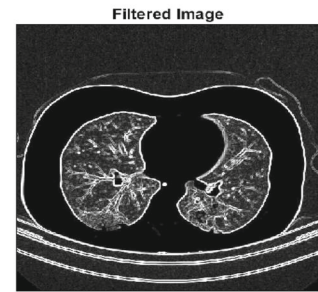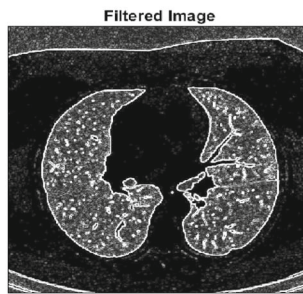

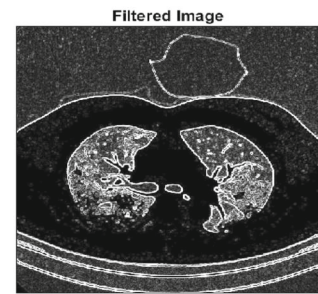**(a)** COVID-19 Patient (Age 35)   **(b)** COVID-19 Patient (Age 40)

(c) COVID-19 Patient (Age 45)   **(d)** COVID-19 Patient (Age 45)

(e) COVID-19 Patient (Age 50)   **(f)** COVID-19 Patient (Age 60)

(g) COVID-19 Patient (Age 65)   **(h)** COVID-19 Patient (Age 70)
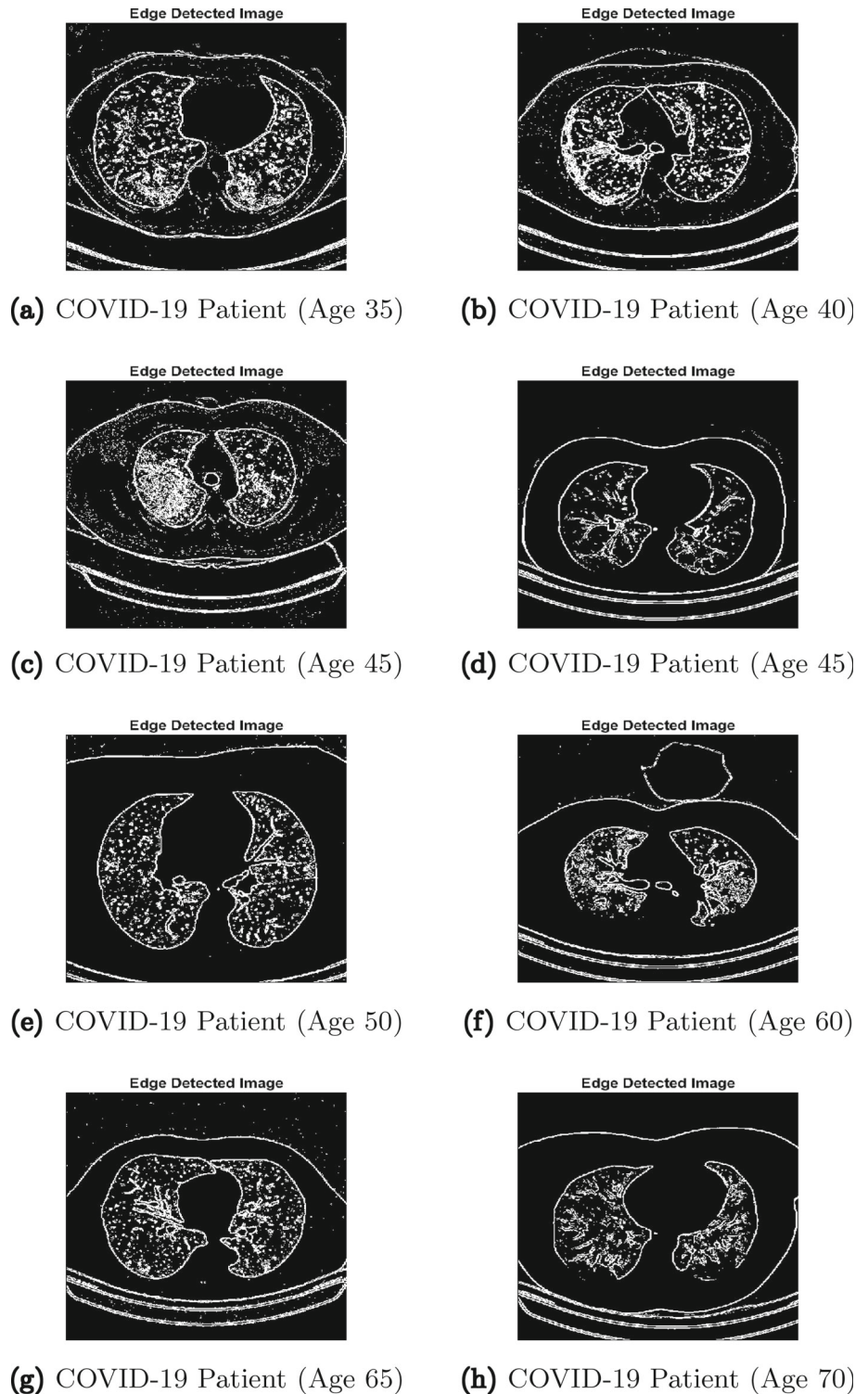
paper, we mainly concentrate on gradient-based operators called the Prewitt, Robert and Sobel operators.

2.4.1 Prewitt method

It is a unique variation operator that estimates the gradient approximation of the image intensity function. In addition, this operator is based on controlling the image with a small separable and integer filter in horizontal and vertical directions. In addition, this operator uses two 3×3 kernels to calculate the approximations of the derivatives attached to the original image [22]. They are one horizontally and the other vertically. They

Fig. 11 Comparison of GFD spectra for filtered COVID-19 patients' CT-scan images using Prewitt, Robert and Sobel methods

(a) COVID-19 Patient (Age 35)

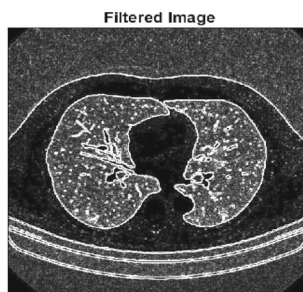**(b)** COVID-19 Patient (Age 40)

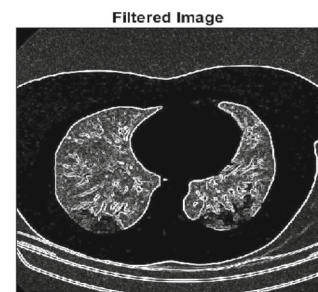**(c)** COVID-19 Patient (Age 45)

(d) COVID-19 Patient (Age 45)

(e) COVID-19 Patient (Age 50)

(f) COVID-19 Patient (Age 60)

(g) COVID-19 Patient (Age 65)

(h) COVID-19 Patient (Age 70)

Fig. 12 Comparison of GFD spectra for edge detected COVID-19 patients' CT-scan images using Prewitt, Robert and Sobel methods
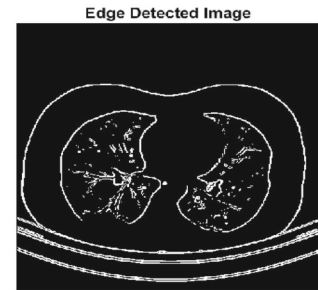

(a) COVID-19 Patient (Age 35)
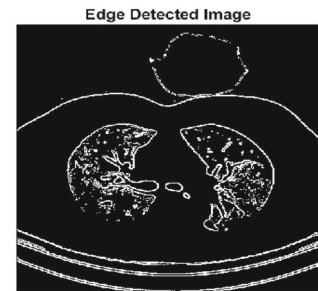
(b) COVID-19 Patient (Age 40)
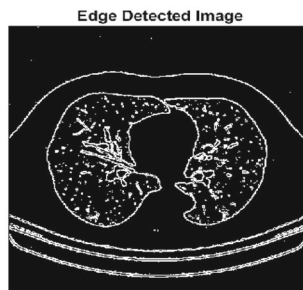
(c) COVID-19 Patient (Age 45)
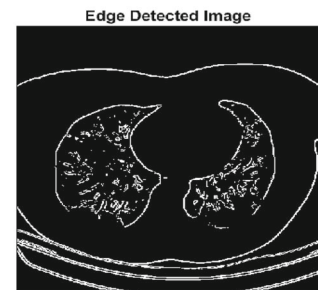
(d) COVID-19 Patient (Age 45)

(e) COVID-19 Patient (Age 50)

(f) COVID-19 Patient (Age 60)

(g) COVID-19 Patient (Age 65)

(h) COVID-19 Patient (Age 70)

3732
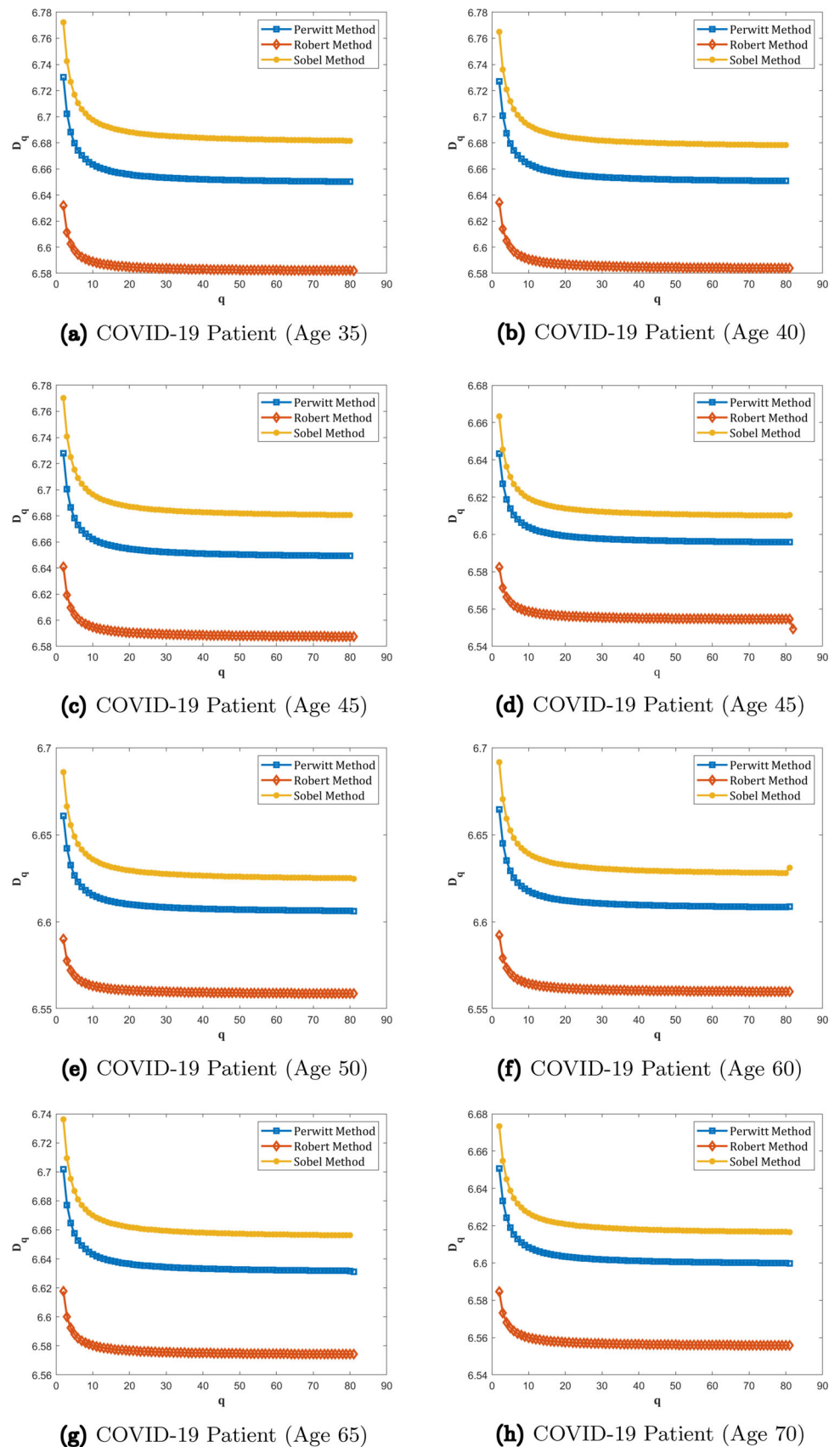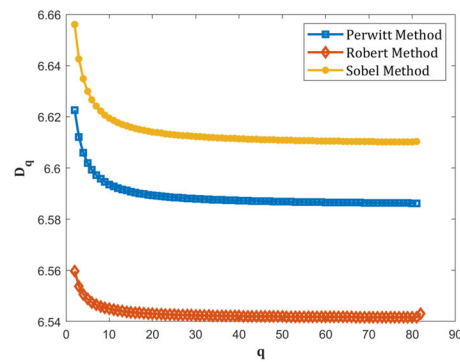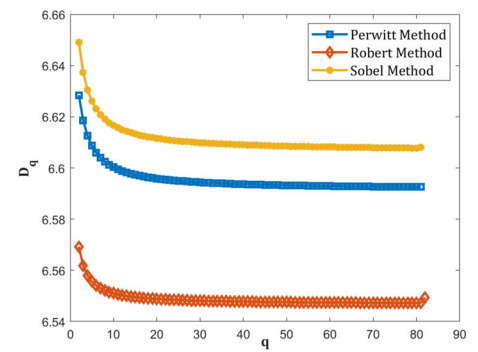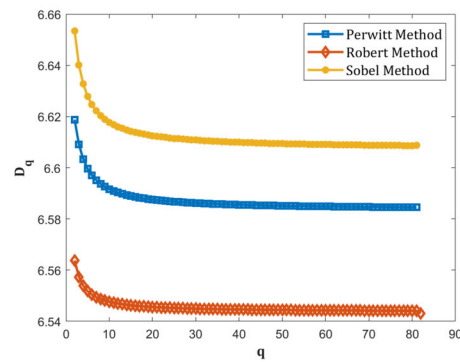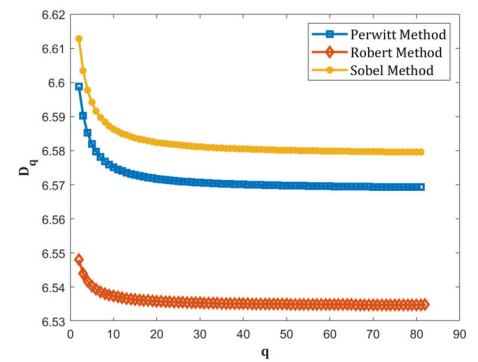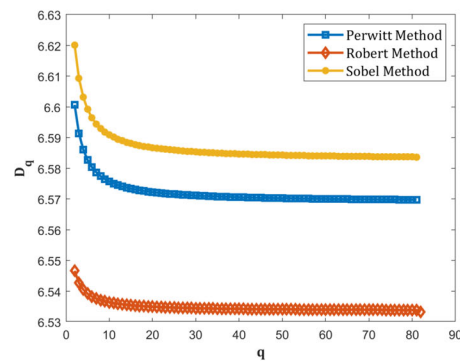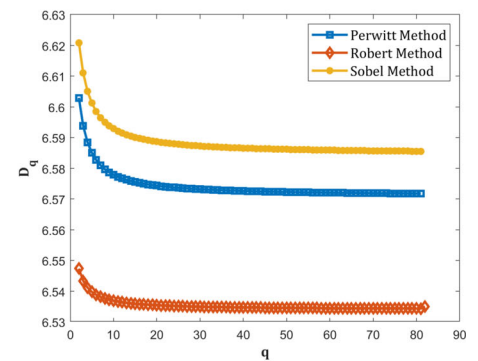
Eur. Phys. J. Spec. Top. (2022) 231:3717–3739
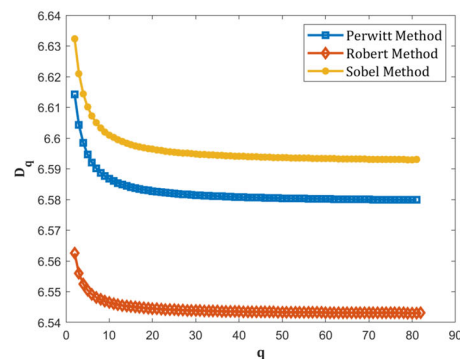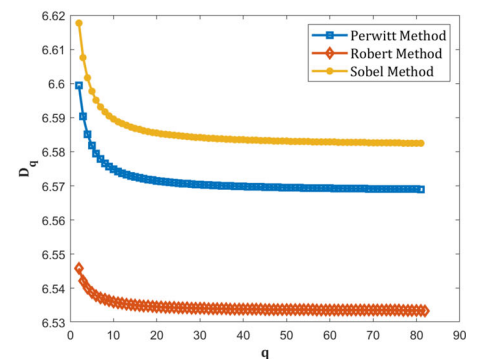
Table 3 Comparison of qualitative measures of Prewitt filtered CT-scan images (Fig. 5) of COVID-19 patients

Patients	SNR	PSNR	MSE	RMSE	SSIM	ESSIM	NSER	EBIQA	EPIQA
P1	11.0317	13.5035	2902.2332	53.8724	0.2805	0.9941	0.7142	1.1393	14.6428
P2	10.9890	13.4268	2953.9045	54.3498	0.2796	0.9941	0.7121	1.0193	14.4461
P3	10.9943	13.4667	2926.9088	54.1009	0.2776	0.9940	0.7167	0.9310	14.3977
P4	10.5558	13.1631	3138.8510	56.0254	0.2068	0.9928	0.7112	0.9312	14.0943
P5	10.7044	13.2943	3045.4585	55.1857	0.2241	0.9933	0.7236	1.0954	14.3896
P6	10.7153	13.3055	3037.6285	55.1147	0.2192	0.9935	0.7019	1.0021	14.3076
P7	10.8049	13.3222	3025.9146	55.0083	0.2547	0.9938	0.7149	1.1434	14.4656
P8	10.6291	13.2358	3086.7305	55.5584	0.2095	0.9929	0.7151	0.9343	14.1701

Table 4 Comparison of qualitative measures of Prewitt edge detected CT-scan images (Fig. 8) of COVID-19 patients

Patients	SNR	PSNR	MSE	RMSE	SSIM	ESSIM	NSER	EBIQA	EPIQA
P1	10.5211	13.0213	3243.003	56.947	0.2217	0.9919	0.8567	0.9805	14.0019
P2	10.5386	13.001	3258.1191	57.07	0.2216	0.9919	0.8600	1.0638	14.0649
P3	10.5053	13.0155	3247.3345	56.9854	0.2116	0.9919	0.8572	0.9234	13.9389
P4	10.4732	13.0742	3203.7709	56.6019	0.1940	0.9917	0.8502	1.0528	14.1270
P5	10.3912	12.9892	3267.1048	57.1586	0.1985	0.9916	0.8468	1.0573	14.0464
P6	10.4716	13.0576	3216.0305	56.7101	0.1966	0.9917	0.8526	1.0853	14.1429
P7	10.4671	13.0052	3255.0780	57.0533	0.2137	0.9918	0.8570	1.2122	14.2174
P8	10.3668	12.9694	3281.9819	57.2886	0.1911	0.9916	0.8485	1.2190	14.1884

Table 5 Comparison of qualitative measures of Robert filtered CT-scan images (Fig. 6) of COVID-19 patients

Patients	SNR	PSNR	MSE	RMSE	SSIM	ESSIM	NSER	EBIQA	EPIQA
P1	10.5102	13.2611	3068.8221	55.3970	0.1889	0.9935	0.6491	1.3959	14.6570
P2	10.5373	13.2716	3061.3677	55.3296	0.1972	0.9936	0.6595	1.6049	14.8765
P3	10.5341	13.2706	3062.1386	55.3366	0.1959	0.9936	0.6511	1.3538	14.6243
P4	10.3684	13.1611	3140.2974	56.0384	0.1488	0.9925	0.6676	0.7689	13.93
P5	10.3174	13.1066	3179.9493	56.3910	0.1536	0.9926	0.6707	0.8892	13.9958
P6	10.3637	13.1529	3146.2362	56.0913	0.1539	0.9928	0.6534	0.7313	13.8841
P7	10.4403	13.1976	3114.0433	55.8036	0.1827	0.9933	0.6625	1.1602	14.3577
P8	10.3018	13.0955	3188.0603	56.4629	0.1459	0.9924	0.6481	0.8373	13.9329

Table 6 Comparison of qualitative measures of Robert edge detected CT-scan images (Fig. 9) of COVID-19 patients

Patients	SNR	PSNR	MSE	RMSE	SSIM	ESSIM	NSER	EBIQA	EPIQA
P1	10.2491	13.0146	3248.0500	56.9917	0.1510	0.9911	0.8431	1.4520	14.4666
P2	10.3265	13.0587	3215.1917	56.7027	0.1711	0.9913	0.8535	1.5450	14.6037
P3	10.3011	13.0519	3220.2352	56.7471	0.1599	0.9912	0.8603	1.4509	14.5028
P4	10.2671	13.0734	3204.3167	56.6067	0.1293	0.9909	0.8331	0.8214	13.8949
P5	10.1937	13.0053	3255.0169	57.0528	0.1283	0.9908	0.8514	0.9012	13.9065
P6	10.1928	13.0016	3257.7751	57.0769	0.1255	0.9907	0.8335	0.8245	13.8261
P7	10.3263	13.0835	3196.9305	56.5414	0.1652	0.9913	0.8502	1.3277	14.4112
P8	10.1579	12.9718	3280.2190	57.2732	0.1177	0.9907	0.8294	0.7896	13.7613

Eur. Phys. J. Spec. Top. (2022) 231:3717–3739

3733

Table 7 Comparison of qualitative measures of Sobel filtered CT-scan images (Fig. 7) of COVID-19 patients

Patients	SNR	PSNR	MSE	RMSE	SSIM	ESSIM	NSER	EBIQA	EPIQA
P1	10.6374	13.3883	2980.2532	54.5917	0.1962	0.9937	0.6459	1.3358	14.7240
P2	10.5016	13.2360	3086.5704	55.5569	0.1947	0.9936	0.6599	1.5894	14.8255
P3	10.5178	13.2542	3073.6794	55.4408	0.1931	0.9936	0.65	1.3289	14.5831
P4	10.3637	13.1564	3143.6893	56.0686	0.1504	0.9925	0.6658	0.922	14.0784
P5	10.3752	13.1645	3137.8463	56.0165	0.1547	0.9927	0.6666	0.819	13.9835
P6	10.2903	13.0795	3199.8711	56.5674	0.1477	0.9926	0.647	0.7192	13.7987
P7	10.4888	13.2461	3079.4647	55.4929	0.1855	0.9934	0.6588	1.1108	14.3569
P8	10.3217	13.1155	3173.4664	56.3335	0.1450	0.9924	0.6510	0.8948	14.0103

Table 8 Comparison of qualitative measures of Sobel edge detected CT-scan images (Fig. 10) of COVID-19 patients

Patients	SNR	PSNR	MSE	RMSE	SSIM	ESSIM	NSER	EBIQA	EPIQA
P1	10.6023	12.9606	3288.6930	57.3471	0.2685	0.9924	0.8592	1.1356	14.0961
P2	10.6502	13.0221	3242.3912	56.9420	0.2536	0.9923	0.8611	1.0830	14.1052
P3	10.7252	13.0922	3190.5401	56.4849	0.2752	0.9926	0.8545	0.9723	14.0644
P4	10.5069	13.0468	3224.0246	56.7805	0.2096	0.9917	0.8620	0.99	14.0368
P5	10.5464	13.0615	3213.1165	56.6844	0.2209	0.9919	0.8498	1.0191	14.0806
P6	10.5114	13.0154	3247.3999	56.9860	0.2072	0.9917	0.8618	0.9763	13.9918
P7	10.5360	12.9961	3261.8636	57.1127	0.2348	0.9922	0.8505	1.1074	14.1035
P8	10.4926	13.0150	3247.7553	56.9891	0.2085	0.9917	0.8619	1.1245	14.1395

can be calculated as follows $G_x = \begin{pmatrix} +1 & 0 & -1 \\ +1 & 0 & -1 \\ +1 & 0 & -1 \end{pmatrix}$ and $G_y = \begin{pmatrix} +1 & +1 & +1 \\ 0 & 0 & 0 \\ -1 & -1 & -1 \end{pmatrix}$. And the gradient is $G(x,y) = \sqrt{G_x^2 + G_y^2}$.

2.4.2 Robert method

Robert is a gradient-based operator. We also use the following 2×2 kernels for the original image to perform this operator edge detection:

$$G_x = \begin{pmatrix} +1 & 0 \\ 0 & -1 \end{pmatrix} \text{and } G_y = \begin{pmatrix} 0 & +1 \\ -1 & 0 \end{pmatrix}.$$

Furthermore, take $I(x, y)$ in the original image and convolve it to the first kernel as G_x and convolve to the second kernel as G_y. Then the gradient can be defined as follows $G(x,y) = \sqrt{G_x^2 + G_y^2}$. Using individual differences, the Robert operator determines the total of the squares of differences between diagonally adjacent pixels [22].

2.4.3 Sobel method

Sobel operator is based on converting images in horizontal and vertical directions with a small, divisible and integer value filter, it is reasonably simple to calculate [22]. The computation is as follows:

$$G_x = \begin{pmatrix} -1 & 0 & +1 \\ -2 & 0 & +2 \\ -1 & 0 & +1 \end{pmatrix} \text{and } G_y = \begin{pmatrix} +1 & +2 & +1 \\ 0 & 0 & 0 \\ -1 & -2 & -1 \end{pmatrix}.$$

Then the gradient can be defined as $G(x,y) = \sqrt{G_x^2 + G_y^2}$.

2.5 Qualitative measures

To analyze the performance of edge detection and denoising process in the medical image processing, the various qualitative measures used in this research study are detailed in this section.

2.5.1 Mean absolute eerror and root mean square error

Mean absolute error (MAE) is the most widely used image quality metric estimator. It is a comprehensive reference metric; therefore, the lower value is better. The MSE is also known as an estimator's mean squared deviation (MSD). The process for measuring an unseen quantity of images is referred to as an estimator. The

3734

Eur. Phys. J. Spec. Top. (2022) 231:3717–3739

Table 9 ANOVA Table for GFD Values of Edge Detected and Filtered CT-scan Images

Source	ss	df	MS	F	Prob¿F
(a) Filtered image for $q = 10$					
Columns	0.0433	2	0.02165	1214.55	1.98097e−22
Error	0.00037	21	0.00002		
Total	0.04368	23			
(b) Filtered image for $q = 20$					
Columns	0.03928	2	0.01964	1145.87	3.63044e−22
Errors	0.00036	21	0.00002		
Total	0.03964	23			
(c) Filtered image for $q = 30$					
Columns	0.03747	2	0.01873	1056.19	8.47386e−22
Errors	0.00037	21	0.00002		
Total	0.03784	23			
(d) Edge detected image for $q = 10$					
Columns	0.02018	2	0.01009	1752.11	4.34365e−24
Errors	0.00012	21	0.00001		
Total	0.0203	23			
(e) Edge detected image for $q = 20$					
Columns	0.01653	2	0.00826	1442.32	3.3058e−23
Errors	0.00012	21	0.00001		
Total	0.01665	23			
(f) Edge detected image for $q = 30$					
Columns	0.01774	2	0.00887	1597.45	1.13929e−23
Errors	0.00012	21	0.00001		
Total	0.01786	23			

MSE or MSD is a calculation that calculates the average square of the errors. The difference between the estimator and the estimated outcome is called the error. It's a risk function that takes into account the squared error loss or quadratic loss's expected value:

$$\mathrm{MAE} = \frac{\sum_{m=1}^{N} \sum_{n=1}^{M} |I_\mathrm{O}(m,n) - I_\mathrm{F}(m,n)|}{M \cdot N}.$$

Root mean square error (RMSE) is possible to measure the difference between the original image and the fragmented image. The RMSE is given as

$$\mathrm{RMSE} = \sqrt{\frac{\sum_{m=1}^{N} \sum_{n=1}^{M} |I_\mathrm{O}(m,n) - I_\mathrm{F}(m,n)|}{M \cdot N}}.$$

2.5.2 Signal–noise ratio

In imaging, the signal-to-noise ratio (SNR) is used to assess image quality. The signal level that creates a threshold level of SNR is often used to define the sensitivity of a (digital or film) imaging system. The signal-to-noise ratio is characterized as follows:

$$SNR = \frac{P_\mathrm{signal}}{P_\mathrm{noise}}$$

where P_signal, P is the average signal value and standard deviation of the signal.

2.5.3 Peak signal–noise ratio

Peak signal–noise ratio (PSNR) is the ratio of the maximum potential signal power to the power of the distorting noise that influences the quality of its representation. The decibel ratio between two images is calculated. Because of the wide dynamic range of the signals, the PSNR is frequently calculated as a decibel scale logarithm term. This dynamic ranges from the highest to the lowest conceivable values, which are affected by their quality. The PSNR can be defined as [19]:

$$\mathrm{PSNR} = 20 \cdot \log\left(\frac{255}{\sqrt{\frac{1}{M \cdot N} \sum_{n=1}^{N} \sum_{m=1}^{M} (I_O(m,n) - I_F(m,n))^2}}\right)$$

where $I_O(m,n)$ and $I_F(m,n)$ indicate the original image and restored image at pixel position (m,n) and M and N are the dimensions of the image.

2.5.4 Structural similarity index

The structural similarity index (SSIM) metric creates a local quality score by combining local image structure, brightness and contrast. After normalizing the brightness and contrast, the structures have patterns of pixel intensity, especially in neighbouring pixels. The SSIM quality metric is very closely aligned with the subjective quality score, because the human display system is capable of perceiving structure [23]. The

$$\text{SSIM} = \text{function}(L(I_1; I_2); C(I_1; I_2); S(I_1; I_2)) \quad (3)$$

where the luminance (L), contrast (C) and structure (S).

2.5.5 Edge-based image quality assessment

One of the most important aspects of human visual judgment is edge preservation. The edge-based image quality assessment (EBIQA) technique is considered to be the most important in the image edge detection [23]. The EBIQA is calculated as

$$\text{EBIQA} = \frac{1}{MN} \sum_{i=1}^{M} \sum_{j=1}^{N} \sqrt{(I_1 - I_2)^2}$$

where $I_1 = (T, A, P, S, \text{SVH}), I_2 = (T, A, P, S, \text{SVH})$ here T is called a total number of edges, A denotes the Average length of edges, P represents the number of pixels with a similar level of intensity values, S is the Sum of pixels in the edges, SVH denotes the sum of pixels, which form edges in either vertically or horizontally located edges.

2.5.6 Edge-based structural similarity

The edge-based structural similarity (ESSIM) the structural similarity components in 2.5.4 can be modified by edge similarity component and mentioned as below [23].

$$\text{ESSIM} = \text{function}(L(I_1; I_2); C(I_1; I_2); E(I_1; I_2)) \quad (4)$$

where $E(I_1; I_2) = \frac{\sigma_{I_1 I_2} + c_3}{\sigma_{I_1} \sigma_{I_2} + c_3}$. Here σ is the standard deviation.

2.5.7 Non-shift edge-based ratio

Non-shift edge-based ratio (NSER) is based on zero crossings. The different standard deviation scales of the

Gaussian kernel system are used to identify interesting images [23]. The NSER can be defined as

$$\text{NSER}(I_1, I_2) = -\sum_{i=1}^{N} \log_{10}(1 - p_i) \quad (5)$$

where $p_i = \|I_1 \cap I_2\| / \|I_1\|$, I_1 and I_2 are reference and tested images.

2.5.8 Edge and pixel-based image quality assessment

The Edge and pixel-based image quality assessment (EPBIQA) is characterized as EPIQA = PSNR + EBIQA.

"In the overall view of the qualitative measures, MSE is basically a weighted function of deviations in images or square differences between the compared images. The main limitation of SSIM measure is the inability to measure the highly blurred images successfully. All the three most common metrics MSE, PSNR, and SSIM are limited in their use for benchmarking the performance of edge detection in the images. Edge preservation is one of the most important aspects of human visual assessment. EBIQA technique aims to operate on the human perception of the features. The IQA technique is the edge-oriented version of the SSIM metric. These qualitative measures for examining images are performed well in their own aspects with the certain limitations."

2.6 ANOVA test

One of the statistical tools for one-way analysis is ANOVA (variance analysis). Average and variance of a particular data set. Variations are used in an ANOVA to determine if the techniques are different. If the observed differences are greater than a certain range, the difference is considered statistically significant. The variance analysis (ANOVA) test can be used to determine the p value. If the p value in this test is close to zero, it raises doubts about the null hypothesis and indicates at least one sample mean. The other sample's mean is completely different.

2.7 Algorithmic structure

The algorithmic flow of the proposed method to calculate the Generalized Fractal Dimension is explained in this section.

Step 1 : Load the test CT-scan images.
Step 2 : Process the image into the GFD method using the median filter method to remove the noise.
Step 3 : Extract the GFD spectra in the original, noisy and denoised images.
Step 4 : Calculating the MAE and PSNR values in the noisy and denoised images.
Step 5 : Apply Prewitt, Robert and Sobel edge detection methods in all the images.

Step 6 : Extract the GFD spectra in the edge detected images.

Step 7 : Calculating the various qualitative measures in the values in the edge detected images.

Step 8 : Finding the ANOVA from the edge detected and filtered images.

3 Experimental data description

In this paper, the CT-scan images of COVID-19 patients with various ages are considered as an experimental images, collected from Societa Italiana di Radiologia Medica e Interventistica (SIRM), Milano, Italy [35]. For the past 8 days, the first patient 35-year-old man suffered from a high temperature, cough, trouble expanding the lungs and dyspnea. The patient also tested positive for coronavirus. After that, the next patient was a 45-year-old man affected by fever, cough, shortness of breath (dyspnea ++) and sore throat. In addition, he was diagnosed with COVID-19. The third patient was a 45-year-old female patient affected by fever, arthralgia, body discomfort, anosmia and dysgeusia plagued for 9 days. COVID-19 was found to be positive after testing. The fourth patient was a 45-year-old female was identify headache, fever, nasal congestion, cough, dyspnoea, pleuritic discomfort, myalgia, loss of smell and taste were experienced by the symptoms in beginning 11 days ago. The COVID-19 testing result was then positive. The next patient, a 50-year-old man with episodic fever, dyspnoea, cough, and odynophagia, tested positive for COVID-19 8 days ago. The remaining patients, a 60-year-old female and a 65-year-old man, had been sick for 3 days and 20 days, respectively, with fever, headache, chest pain, and breathing difficulties and had tested positive for COVID-19. Finally, the 70-year-old man 5 days ago affected the symptoms of fever, cough, myalgia and mild hypoxemia. COVID-19 was found to be positive after testing. Table 1 describes the details of the patients. In addition, Fig. 1 shows the COVID-19 patient's sample set of original CT-scan images.

4 Results and discussion

We first converted the CT-scan images of patients suffering from various COVID-19 infections into 0.05 magnitude salt and pepper noise, which is clearly shown in Fig. 2. The modified noise images are then denoised with median filtering, as illustrated by Fig. 3. For the second step were computed the Generalized Fractal Dimension spectra were to the original, noise and denoised images.

Figure 4 clearly shows the Generalized Fractal Dimension spectra graphically of the original, noise and denoised images of all COVID-19 patients. It is also clear that the complexity of the noise images is higher in most images than in their original images, and that the complexity of the denoised CT-scan images is often less or equal to that of the original images.

Table 2 also differentiates the two qualitative measures MAE and PSNR for noise and denoised images of all COVID-19 patients. In it, we found MAE and PSNR values using salt and pepper noise at 0.05, respectively, for patient images. The MAE value of the noise-generated images is greater than the value of the denoised images and the PSNR value of the noise-generated images is less than the value of the denoised images. From this, the median filter is one of the best methods to denoise the images.

Next, we use some of the sample COVID-19 patients to analyze the images of three types of edge detection methods. These are the Prewitt, Robert and Sobel edge detection methods. Figures 5, 6 and 7 shows the Prewitt, Robert and Sobel filtered images, respectively. In addition, Figs. 8, 9 and 10 shows Prewitt, Robert and Sobel Edge Detection, respectively.

Converting the original images into filtered and edge detected images using the Prewitt, Robert and Sobel edge detection method. After that compute the GFD spectrum of images is calculated by the Prewitt, Robert and Sobel edge detected images and the filtered images.
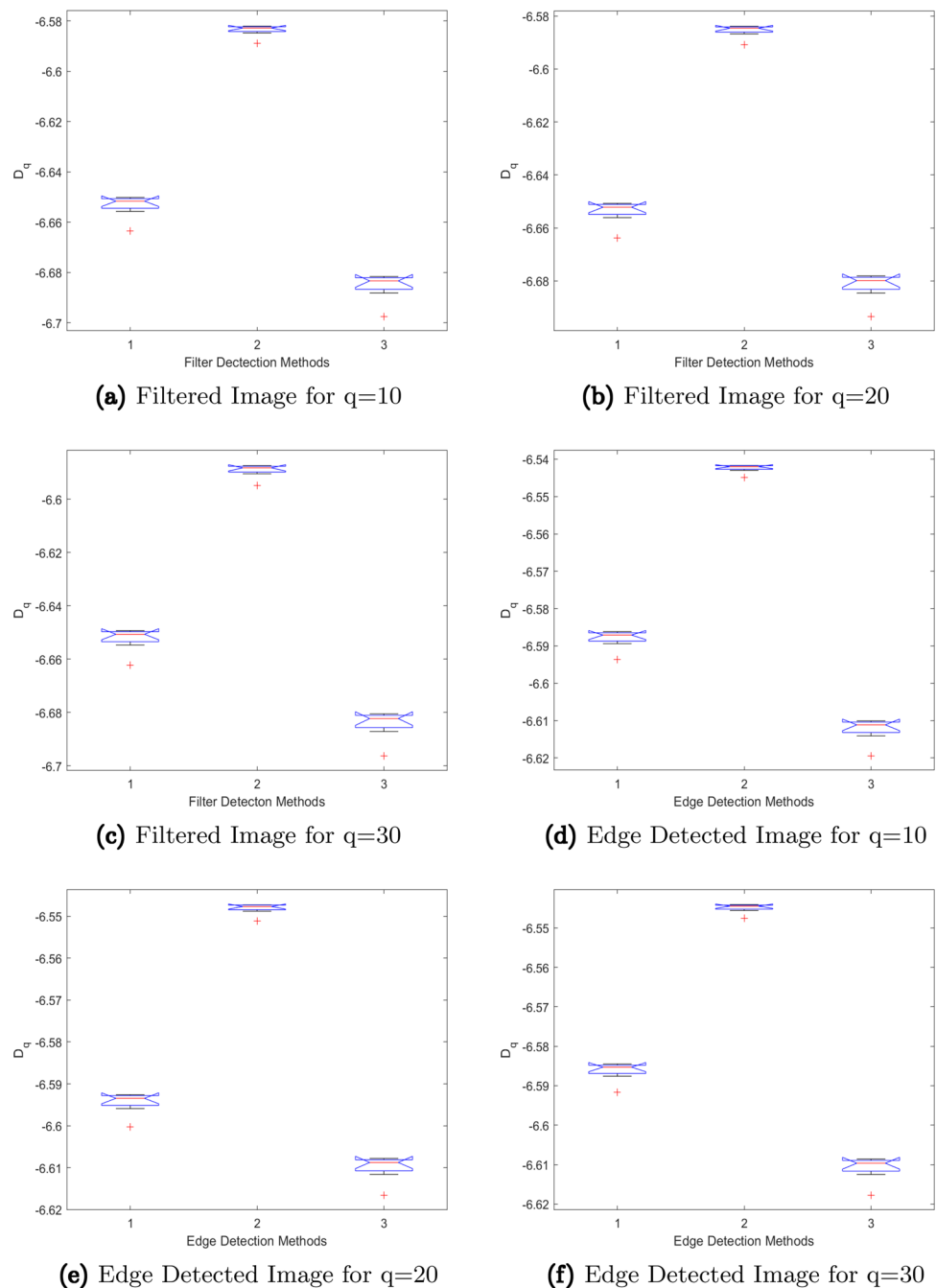
The detected GFD spectra are clearly depicted graphically in Fig. 11. In addition, in Fig. 11 the image of GFD spectra up to Fig. 11a–h shows that the value of D_q decreases to increase the value of q, respectively. While the other two filtered GFD spectra curve is higher than the GFD spectra of Robert filtered images. In addition, based on this it is clear that Prewitt filtered and Sobel filtered images have more complexity than Robert filtered images. In addition, Sobel filtered images to make it clear that they are more complex than the other two images. Finally, their probability distributions for all patient images were obtained according to their q values.

The detected GFD spectra are clearly shown graphically in Fig. 12. In addition, in Fig. 12 the image of GFD spectra up to Fig. 12a–h shows that the value of D_q decreases to increase the value of q, respectively. While the other two edges detected GFD spectra curves are higher than the GFD spectra of Robert edge detected images. In addition, based on this it is clear that Prewitt edge detected and Sobel edge detected images have more complexity than Robert edge detected images. In addition, Sobel edge detected images make it clear that they are more complex than the other two images. Finally, their probability distributions for all patient images were obtained according to their q values.

Tables 3, 4, 5, 6, 7 and 8 calculate the values of different quality metrics of filtered and edge detected images 5–10 of the three methods Prewitt Method, Robert Method and Sobel Method. Based on Tables 3 and 6, Tables 4 and 7, Tables 5 and 8, the filtered image quality metric values are better than the edge metric values. In this thought, we conclude that the filtered image is less complex than the edge detected image comparatively.

In addition, Tables 3, 4, 5, 6, 7 and 8 show that the Prewitt, Robert and Sobel filtered and Edge methods

Fig. 13 Notched box plots for generalized fractal spectra of edge detected and filtered CT-scan images of COVID-19 patients

(a) Filtered Image for q=10

(b) Filtered Image for q=20

(c) Filtered Image for q=30

(d) Edge Detected Image for q=10

(e) Edge Detected Image for q=20

(f) Edge Detected Image for q=30

are slightly smaller in value compared to the qualitative measures. The graphical system of the GFD spectra is the easiest way to differ the image complexity.

ANOVA Test also supports our designed methods statistically, than the GFD Method. The p value in Table 9a is greater than the p values in Table 9b, c, which are less to the first table value. In addition, the p value in Table 9c is greater than the p values in Table 9a, b, which are less to the first table value. Hence the values are evidence that GFD spectra analysis is the way to get the comparison of the edge detected and filtered images easily.

In the line of above observations from COVID-19 patients, the CT-scan images analysis using filtering

and edge detection methods along withe GFD measure are clearly presented in Table 3, 4, 5, 6, 7 and 8. It is evidently shows that, the Sobel method is significantly with high GFD values compare to the GFD curves for other methods. Aside, the qualitative measure values in Tables 3, 4, 5, 6, 7 and 8 and the values in the statistical Tables 9 rapidly increased in the Sobel method for representative images. It is concluded that the Sobel method is executed well with more information on the considered experimental grayscale images at edge detected and filtered categories. Thus, the Sobel-based processed CT-scan lung images may help us to identify infection rate of COVID-19 patients.

3738

Eur. Phys. J. Spec. Top. (2022) 231:3717–3739

Likewise, as in Fig. 13, the box plots of range values of fractal spectra for the GFD method among Prewitt, Robert and Sobel filtered and Edge detected images data are achieved that there is significant variability in the fractal spectra of all our designed methods among the Prewitt, Robert and Sobel filtered and Edge detected image as compared with the GFD method.

5 Conclusion

In this context, the multifractal theory is applied to evaluate the CT-scan images of COVID-19 patients with different age levels. Initially, the proposed scheme converts the representative original images in noisy images by introducing the salt and pepper noise with density 0.05 units. Those corrupted images are denoised by the median filtering techniques. Then, the GFD spectra is computed for all types of original, noisy and denoised CT-scan grayscale images and depicted the GFD curve for all images graphically to compare the complexity in terms of noise levels in original, noisy and denoised categories. To ensure the same, the performance measures MAE and PSNR values are calculated and tabulated to prove the classification by GFD spectra. At the second part of the proposed method, the three edge detection algorithms such as Robert, Prewitt, and Sobel are applied and obtained the filtered and edge detected CT-scan images. Furthermore, the GFD spectra is constructed for all categories of filtered and edge detected images and depicted graphically. From the obtained results, the multifractal measure significantly discriminates the original, noisy & denoised images and also the filtered and edge detected images. The qualitative measures of all types of images gained from three edge detection methods are portrayed and analyzed their performances. It is concluded that GFD-based classification along with the qualitative measures expose that Sobel method performed well in terms of edge detection. At last, the same classification rate is supported statistically by the ANOVA test and box plots. It is hopefully viewed that the proposed comparative analysis using multifractal and edge detection methods will be useful to sense the infection level of lungs for COVID-19 patients.

Data availability statement This manuscript has associated data in a data repository [Authors' comment: Data are publicly released by SIRM - Societa Italiana di Radiologia Medica e Interventistica (Italian Society of Medical and Interventional Radiology), at http://sirm.org/category/COVID-19/, [35]].

References

1. B.B. Mandelbrot, *The Fractal Geometry of Nature* (W.H. Freeman and Company, New York, 1983)
2. M.F. Barnsley, *Fractals Everywhere* (Academic Press, USA, 2014)
3. M.F. Barnsley, *SuperFractals* (Cambridge University Press, New York, 2006)
4. K. Falconer, *Fractal Geometry: Mathematical Foundations and Applications* (Wiley, England, 2003)
5. G. Edgar, *Measure, Topology, and Fractal Geometry* (Springer, New York, 2008)
6. P. Grassberger, Phys. Lett. A **97A**(6), 227–230 (1983)
7. H.G.E. Hentschel, I. Procaccia, Physica **8D**(3), 435–444 (1983)
8. D. Easwaramoorthy, R. Uthayakumar, J. Comput. Sci. **2**(1), 31–38 (2011)
9. R. Uthayakumar, D. Easwaramoorthy, Fluct. Noise Lett. **11**(4), 1250034 (2012)
10. R. Uthayakumar, D. Easwaramoorthy, Fractals **21**(2), 1350011 (2013)
11. S. Dai, K. Sun, S. He, W. Ai, Entropy **21**(11), 1115 (2019)
12. B. Yan, S. He, K. Sun, Entropy **21**(9), 849 (2019)
13. B. Yan, S. Mukherjee, S. He, Eur. Phys. J. Spec. Top. **228**, 2769–2777 (2019)
14. S. Banerjee, M.K. Hassan, S. Mukherjee, A. Gowrisankar, *Fractal Patterns in Nonlinear Dynamics and Applications* (CRC Press, Boca Raton, 2020)
15. S. Banerjee, D. Easwaramoorthy, A. Gowrisankar, *Fractal Functions, Dimensions and Signal Analysis (Understanding Complex Systems, Springer: Complexity* (Springer, Cham, 2021)
16. D. Easwaramoorthy, A. Gowrisankar, A. Manimaran, S. Nandhini, L. Rondoni, S. Banerjee, Nonlinear Dyn. **106**(2), 1375–1395 (2021)
17. Q. Rong, C. Thangaraj, D. Easwaramoorthy, S. He, Eur. Phys. J. Spec. Top **230**, 3947–3954 (2021)
18. N.M. Rasheed, M.O. Al-Amr, E.A. Az-Zobi, M.A. Tashtoush, L. Akinyemi, Mathematics **9**(16), 1986 (2021)
19. R.C. Gonzalez, R.E. Woods, S.L. Eddins, *Digital Image Processing Using MATLAB* (Gatesmark Publishing, USA, 2020)
20. J. Chauveau, D. Rousseau, P. Richard, F. Chapeau-Blondeau, Chaos Solitons Fract. **43**, 57–67 (2010)
21. T. Chen, M. Kai-Kuang, L.H.C. Chen, IEEE Trans. Image Process. **8**(12), 1834–1838 (1999)
22. S.R. Hait, R. Mesiar, P. Gupta, D. Guha, D. Chakraborty, Inf. Fusion **80**, 226–240 (2022)
23. D. Sadykova, A.P. James, International Conference on Advances in Computing, Communications and Informatics (ICACCI), IEEE, (2017), pp. 2366–2369
24. Q. Ding, P. Lu, Y. Fan, Y. Xia, M. Liu, J. Med. Virol. **92**(9), 1549–1555 (2019)
25. E. Mahase, NEWS, BMJ Publishing Group Limited, London (2020)
26. M. Kojicic, E. Festic, O. Gajic, Bosnian J. Basic Med. Sci. **9**, 8 (2009)
27. D.H. Dockrell, M. Moira, K.B. Whyte, T.J. Mitchell, Chest **142**(2), 482–491 (2012)
28. Y.G. Son, J. Shin, H.G. Ryu, J. Dent. Anesthesia Pain Med. **17**(1), 1–12 (2017)
29. A.L. Laurila, L. Von Hertzen, P. Saikku, Scand. J. Infect. Dis. Suppl. **104**, 34–36 (1997)
30. C.L. Kiew, A. Brahmananda, K.T. Islam, H.N. Lee, S.A. Venier, A. Saraar, H. Namazi, Fractals **28**(1), 2050019 (2020)
31. N. Tanabe, S. Muro, S. Sato, T. Oguma, A. Sato, T. Hirai, BMC Pulmon. Med. **18**(1), 5 (2018)

Eur. Phys. J. Spec. Top. (2022) 231:3717–3739

3739

32. H. Namazi, V.V. Kulish, Fractals **28**(05), 2050114 (2020)
33. H. Namazi, Fractals **28**(07), 2050129 (2020)
34. B. Astinchap, H. Ghanbaripour, R. Amuzgar, Chaos Solitons Fract. **5**, 111820 (2022)
35. SIRM-Societa Italiana di Radiologia Medica e Interventistica (2022), https://sirm.org/category/COVID-19/